partial differential equations (PDEs) problems. The derivability and accuracy of MQ allow the construction of large systems of equations, where a function and its derivatives appear all at once. This method showed its efficacy in a variety of applications, involving both global [20]-[22] and local [23]-[25] RBF. Despite its versatility, Fasshauer [26] pointed out drawbacks of this strategy such as the asymmetry of the associated matrix and its singularity for certain arrangements of points, proposing a Hermitian form able to overcome these issues.

Collocation methods are not the only way to adopt RBF in a meshless solution process. The method of fundamental solutions (MFS) [27] as well as the dual reciprocity method (DRM) [28] can adopt RBF to handle various problems, with no mesh involved. In [29] and [30] RBF substitute classical shape functions for the local approximation task while a background mesh is still necessary to integrate the Galerkin weak form.

Without the need of connectivity, meshless methods are particularly suitable for studies in which geometry changes also involve internal boundaries. For this reason, several notable examples of fracture mechanics problems tackled by using meshless methods can be encountered in literature [31][32][33].

In [34], Belytschko *et al.* proposed the element free Galerkin (EFG) method to model crack propagation. The EFG is extensively employed in literature given its high accuracy in the solution of elliptic problems. In [35] Khosravifard *et al.* employed the EFG method and meshless radial point interpolation, together with the background decomposition method (BDM) to obtain the integral form of a fracture mechanics problem. A local partition of unity method was proposed in [36] to be used with EFG for the analysis of quasi-static 2D crack growth. In [37] YuanTong *et al.* proposed an enriched radial basis function (e-RPIM) method for the accurate description of crack tip fields, including stress and displacement. In [38] Biancolini *et al.* employed RBF splines for the deformation of the numerical FEM domains employed for the stress intensity factor (SIF) calculations, relying on 2D crack development models and furtherly expanding the concept for multi degree of freedom problems in [39].

The authors recently proposed a method to improve FEM results obtained for 2D models [40]. FEM displacements are continuous across elements and exhibit a faster h-convergence with respect to their derived fields [7]. RBF interpolation of FEM displacements provides a continuous analytical form over the domain. Strain and stress fields obtained from derivation of the RBF interpolator do not suffer from the continuity problems typical of shape functions, showing a higher accuracy with respect to FEM. Proposed method proved to give the greatest benefit when coarse meshes are considered, improving FEM results in correspondence of stress raisers. In [41] authors moved a step forward, exploiting the continuous and differentiable representation of the scattered FEM displacements obtained using RBF. By adding RBF points to the preexistent FEM nodes, local imbalance was reduced while maintaining the original values on the FEM nodes, obtaining straightforwardly the stress and strain values. In the present work, the approach demonstrated in [41] is applied in fracture mechanics as a post-processing tool for Q1 FEM models, enriching numerical results with RBF points in a meshless fashion. An analytical meshless RBF-based procedure to extract the J-integral value is employed on such obtained results, exploiting the analytical differentiability of RBF. Using this method, crack analysis can be performed on coarse numerical meshes with linear elements, otherwise not suitable for fracture mechanics applications. Additional RBF points are added only where needed and in a second time after structural analysis, performing the J-integral calculation in the interested area, obtaining results comparable to the ones achieved using parabolic elements. The paper is structured as described: after a first mathematical introduction on RBF, the numerical procedure at the basis of this work is illustrated. The approach is then validated on two structural cases with strong stress concentrations prior to the application on a mode I crack opening simulation for the J-integral evaluation by means of the proposed method.

II. Radial Basis Functions

Radial basis functions interpolation is a subject covered in many dedicated textbooks, from either a mere mathematical [42] or a more applicative perspective [43]. RBF have given their contribution in a wide range of fields pertaining to engineering and science: neural networks [44] to computer graphics (surface reconstruction [45]), mesh morphing [46][47] to image analysis of deformations [48] and data transfer [49]. RBF mesh morphing has been employed for several applications, from FSI coupling [50] to genetic [51], evolutionary optimizations [52] and advanced modelling [53].

Let suppose to have a set of N points $\boldsymbol{x_i}$ with i=1,…,N in $\mathbb{R}^d$ for which the scalar values g_i are assigned. A RBF interpolant $s(\boldsymbol{x})$ is a series of radial basis φ, biased by the weights γ_i:

$$s(x) = \sum_{i=1}^{N} \gamma_i \varphi(\|x - x_i\|) \quad (1)$$

Two significant benefits of RBF interpolation are clear from the above expression:

1) Interpolation is constructed just in terms of nodes.
2) The Euclidean norm reduces the original space dimension to a scalar quantity, providing dimensional independence.

Typical RBF kernels are shown in Table 1 with $r = \|\boldsymbol{x} - \boldsymbol{x_i}\|$, ϵ is a shape parameter [54], which should depend upon the average grid spacing. Given the expressions in Table 1, it is worth to notice that the generalized multiquadratic can assume also the form of any spline, multiquadratic, inverse multiquadratic and inverse quadratic kernel with a proper choice of the exponent q and of the parameter R.

The coefficients γ_i are such that the interpolator $s(\boldsymbol{x})$ gives exactly the values g_i at the original (source) points $\boldsymbol{x_i}$. In matrix form:

$$\boldsymbol{M\gamma} = \boldsymbol{g} \quad (1)$$

The matrix $\boldsymbol{M}$ collects the radial basis φ computed at the source points and its inversion is necessary to determine the

vector of weights $\boldsymbol{\gamma}$. Sometimes it is convenient to add a polynomial supplement $h(\mathbf{x})$ to the expression in (1), in this way polynomial functions of the same form of $h(\mathbf{x})$ can be reproduced exactly. This comes at the cost of a formal complication of the system in (2), anyway in the present work we make no use of the polynomial supplement thus no more details are given in this regard.

It seems suitable to continue this brief dissertation on RBF, rather general so far, directly addressing the workflow presented in this paper. In the specific context, RBF reproduce two-dimensional displacement fields. Thus, it is appropriate to illustrate the case of RBF interpolating a vector field in 2D. As the RBF interpolation works on scalar functions, each component of the displacement field requires its RBF series:

$$\begin{cases} u = s_x(\mathbf{x}) = \sum_{i=1}^{N} \gamma_i^x \varphi\left(\|\mathbf{x}-\mathbf{x}_i\|\right) \\ v = s_y(\mathbf{x}) = \sum_{i=1}^{N} \gamma_i^y \varphi\left(\|\mathbf{x}-\mathbf{x}_i\|\right) \end{cases} \tag{2}$$

Strain is the symmetric part of the gradient of the vector field of (3) and is the result of a differentiation procedure. Radial basis are derivated with respect to x and y. Taking the example of the GMQ kernel, it is straightforward to apply the chain rule which yields

$$\begin{aligned} \frac{\partial s(\mathbf{x})}{\partial x} &= \sum_{i=1}^{N} \gamma_i \cdot q(\epsilon^2 r^2 + R^2)^{q-1} 2\epsilon^2 (x - x_i) \\ \frac{\partial s(\mathbf{x})}{\partial y} &= \sum_{i=1}^{N} \gamma_i \cdot q(\epsilon^2 r^2 + R^2)^{q-1} 2\epsilon^2 (y - y_i) \end{aligned} \tag{3}$$

The differentiation procedure recurs as many times as the degree of derivative required. Differential equations of balance contain second degree derivatives of the components of displacement, thus the differentiation rule must be repeated twice.

Table 1 most common radial basis functions

RBF	$\boldsymbol{\varphi(r)}$
Spline type (Rn)	$r^n, n\ odd$
Thin plate spline (TPSn)	$r^n \log(r), n\ even$
Multiquadratic (MQ)	$\sqrt{1+\epsilon^2 r^2}$
Inverse multiquadratic (IMQ)	$\frac{1}{\sqrt{1+\epsilon^2 r^2}}$
Inverse quadratic (IQ)	$\frac{1}{1+\epsilon^2 r^2}$
Gaussian (GS)	$e^{-\epsilon^2 r^2}$
Generalized multiquadratic (GMQ)	$(\epsilon^2 r^2 + R^2)^q$

III. Numerical Procedure

This paper presents a progress with respect to the former work detailed in [40]. For sake of completeness, the following points outline the referenced method:

1) Several 2D structural cases of stress concentration were solved via FEM.
2) RBF interpolation supplied a smooth form of the displacement field, starting from FEM nodal values.
3) Analytical differentiation of the interpolated displacements provided the strain field.
4) Application of Hook's law supplied the stress map throughout the model, which proved to be more accurate than that provided by FEM for the same case.

The mentioned paper also showed the convergence of the method when increasing the level of mesh refinement up to a very dense discretization.

The progress developed here consists in including local balance in the RBF interpolator. As in [40], we still consider two-dimensional plane stress problems. The material is homogeneous and isotropic. Under these assumptions, Hook's law relates stress to strain vector as follows:

$$\begin{Bmatrix} \sigma_x \\ \sigma_y \\ \tau_{xy} \end{Bmatrix} = \begin{bmatrix} \frac{E}{1-\nu^2} & \frac{\nu E}{1-\nu^2} & 0 \\ \frac{\nu E}{1-\nu^2} & \frac{E}{1-\nu^2} & 0 \\ 0 & 0 & G \end{bmatrix} \begin{Bmatrix} \varepsilon_x \\ \varepsilon_y \\ \varepsilon_{xy} \end{Bmatrix} \tag{4}$$

where E is the Young modulus, ν is the Poisson coefficient and the shear modulus is

$$G = \frac{E}{2(1+\nu)} \tag{5}$$

Displacement derivatives form the strain components:

$$\begin{aligned} \varepsilon_x &= \frac{\partial u}{\partial x} \\ \varepsilon_y &= \frac{\partial v}{\partial y} \\ \varepsilon_{xy} &= \frac{\partial u}{\partial y} + \frac{\partial v}{\partial x} \end{aligned} \tag{6}$$

Stresses inside the material should satisfy equilibrium equations, with no body force applied and for 2D plane stress cases, they assume the form:

$$\begin{aligned} \frac{\partial \sigma_x}{\partial x} + \frac{\partial \tau_{xy}}{\partial y} &= 0 \\ \frac{\partial \tau_{xy}}{\partial x} + \frac{\partial \sigma_y}{\partial y} &= 0 \end{aligned} \tag{7}$$

Plugging (5)-(7) in (8), equilibrium equations can be written in terms of displacement derivatives:

$$\begin{aligned} \frac{1}{1-\nu}\left(\frac{\partial^2 u}{\partial x^2} + \nu \frac{\partial^2 v}{\partial x \partial y}\right) + \frac{1}{2}\left(\frac{\partial^2 u}{\partial y^2} + \frac{\partial^2 v}{\partial x \partial y}\right) &= 0 \\ \frac{1}{2}\left(\frac{\partial^2 u}{\partial x \partial y} + \frac{\partial^2 v}{\partial x^2}\right) + \frac{1}{1-\nu}\left(\frac{\partial^2 v}{\partial y^2} + \nu \frac{\partial^2 u}{\partial x \partial y}\right) &= 0 \end{aligned} \tag{8}$$

RBF interpolation provides u and v in a continuous and differentiable form. Coefficients vectors $\boldsymbol{\gamma}^x$ and $\boldsymbol{\gamma}^y$ allow expressing the components of displacement as RBF series (see (3)).

They come from the inverse problems:

$$\boldsymbol{\gamma^x = M^{-1}u}$$
$$\boldsymbol{\gamma^y = M^{-1}v} \quad (9)$$

Vectors $\boldsymbol{u}$ and $\boldsymbol{v}$ contain the scattered data from which interpolation starts. The aim of the proposed method is to embed local balance in the series form of (3), retaining nodal displacements. Bearing this in mind, global vectors must contain displacements both at FEM nodes and in correspondence of new sites, whose associated values minimize error on balance. Let N_F and N_a be the number of FEM nodes and added points respectively, we pose

$$\boldsymbol{u = u_0 + Su_a}$$
$$\boldsymbol{v = v_0 + Sv_a} \quad (10)$$

The row-vectors $\boldsymbol{u_0}$ and $\boldsymbol{v_0}$ have dimension N_F+N_a, with FEM nodal displacements in the first N_F positions and zero afterwards. The vectors $\boldsymbol{u_a}$ and $\boldsymbol{v_a}$ contain the N_a values of displacement at additional points. The matrix $\boldsymbol{S}$ concatenates displacements in order to assemble the global vectors. It consists of two sub-matrices:

$$\boldsymbol{S} = \begin{bmatrix} \boldsymbol{0} \\ \boldsymbol{I} \end{bmatrix} \quad (11)$$

The matrix $\boldsymbol{0}$ is all-zeros $N_F \times N_a$, $\boldsymbol{I}$ is the identity matrix with dimension $N_a \times N_a$. Plugging (11) in (10) we obtain

$$\boldsymbol{\gamma^x = M^{-1}u_0 + M^{-1}Su_a}$$
$$\boldsymbol{\gamma^y = M^{-1}v_0 + M^{-1}Sv_a} \quad (12)$$

RBF interpolation supplies the displacement field in a smooth form, for which derivation only acts on the matrix $\boldsymbol{M}$ of radial basis. The notations $\partial \boldsymbol{M}$ and $\partial^2 \boldsymbol{M}$ adopted below indicate the matrices containing the first and second order derivatives of the terms in $\boldsymbol{M}$, computed at all the points of the system (i.e. FEM nodes and additional sites). We state the following equalities

$$\boldsymbol{q_x} = \frac{1}{1-\nu}\left(\frac{\partial^2 \boldsymbol{M}}{\partial x^2}\boldsymbol{M^{-1}u_0} + \nu\frac{\partial^2 \boldsymbol{M}}{\partial x \partial y}\boldsymbol{M^{-1}v_0}\right) + \\ + \frac{1}{2}\left(\frac{\partial^2 \boldsymbol{M}}{\partial y^2}\boldsymbol{M^{-1}u_0} + \frac{\partial^2 \boldsymbol{M}}{\partial x \partial y}\boldsymbol{M^{-1}v_0}\right) \quad (13)$$

$$\boldsymbol{q_y} = \frac{1}{2}\left(\frac{\partial^2 \boldsymbol{M}}{\partial x \partial y}\boldsymbol{M^{-1}u_0} + \frac{\partial^2 \boldsymbol{M}}{\partial x^2}\boldsymbol{M^{-1}v_0}\right) + \\ + \frac{1}{1-\nu}\left(\frac{\partial^2 \boldsymbol{M}}{\partial y^2}\boldsymbol{M^{-1}v_0} + \nu\frac{\partial^2 \boldsymbol{M}}{\partial x \partial y}\boldsymbol{M^{-1}u_0}\right) \quad (14)$$

$$\boldsymbol{R_x} = \frac{1}{1-\nu}\frac{\partial^2 \boldsymbol{M}}{\partial x^2}\boldsymbol{M^{-1}S} + \frac{1}{2}\frac{\partial^2 \boldsymbol{M}}{\partial y^2}\boldsymbol{M^{-1}S} \quad (15)$$

$$\boldsymbol{R_y} = \frac{1}{2}\frac{\partial^2 \boldsymbol{M}}{\partial x^2}\boldsymbol{M^{-1}S} + \frac{1}{1-\nu}\frac{\partial^2 \boldsymbol{M}}{\partial y^2}\boldsymbol{M^{-1}S} \quad (16)$$

$$\boldsymbol{T} = \frac{1}{2}\frac{\partial^2 \boldsymbol{M}}{\partial x \partial y}\boldsymbol{M^{-1}S} + \frac{1}{1-\nu}\frac{\partial^2 \boldsymbol{M}}{\partial x \partial y}\boldsymbol{M^{-1}S} \quad (17)$$

Using (14)-(18), residuals of balance equations (9) assume the compact form

$$\boldsymbol{e_x = R_x u_a + T v_a + q_x}$$
$$\boldsymbol{e_y = R_y v_a + T u_a + q_y} \quad (18)$$

We consider the sum of the squared norms of $\boldsymbol{e_x}$ and $\boldsymbol{e_y}$ as a measure of the overall error on balance e:

$$\|\boldsymbol{e_x}\|^2 = (\boldsymbol{R_x u_a + T v_a + q_x})^T(\boldsymbol{R_x u_a + T v_a + q_x})$$
$$\|\boldsymbol{e_y}\|^2 = (\boldsymbol{R_y v_a + T u_a + q_y})^T(\boldsymbol{R_y v_a + T u_a + q_y}) \quad (19)$$

$$e = \|\boldsymbol{e_x}\|^2 + \|\boldsymbol{e_y}\|^2 \quad (20)$$

Sought vectors $\boldsymbol{u_a}$ and $\boldsymbol{v_a}$ are those that minimize e:

$$\begin{cases} \dfrac{\partial e}{\partial \boldsymbol{u_a}} = \boldsymbol{0} \\ \dfrac{\partial e}{\partial \boldsymbol{v_a}} = \boldsymbol{0} \end{cases} \quad (21)$$

For sake on conciseness, we adopt

$$\boldsymbol{p_x} = -(\boldsymbol{R_x}^T\boldsymbol{q_x} + \boldsymbol{T}^T\boldsymbol{q_y}) \quad (22)$$

$$\boldsymbol{p_y} = -(\boldsymbol{R_y}^T\boldsymbol{q_y} + \boldsymbol{T}^T\boldsymbol{q_x}) \quad (23)$$

$$\boldsymbol{Q_x} = \boldsymbol{R_x}^T\boldsymbol{R_x} + \boldsymbol{T}^T\boldsymbol{T} \quad (24)$$

$$\boldsymbol{Q_y} = \boldsymbol{R_y}^T\boldsymbol{R_y} + \boldsymbol{T}^T\boldsymbol{T} \quad (25)$$

$$\boldsymbol{D_x} = -(\boldsymbol{R_x}^T\boldsymbol{T} + \boldsymbol{T}^T\boldsymbol{R_y}) \quad (26)$$

$$\boldsymbol{D_y} = -(\boldsymbol{R_y}^T\boldsymbol{T} + \boldsymbol{T}^T\boldsymbol{R_x}) \quad (27)$$

Equations (23)-(28) allow to express $\boldsymbol{u_a}$ and $\boldsymbol{v_a}$ in the short form

$$\boldsymbol{u_a} = (\boldsymbol{Q_x - D_x Q_y^{-1} D_y})^{-1}(\boldsymbol{D_x Q_y^{-1} p_y + p_x})$$
$$\boldsymbol{v_a} = (\boldsymbol{Q_y - D_y Q_x^{-1} D_x})^{-1}(\boldsymbol{D_y Q_x^{-1} p_x + p_y}) \quad (28)$$

It is worth to notice that the matrices $\boldsymbol{Q_x}$and $\boldsymbol{Q_y}$ and their inverse forms are symmetric, given (25) and (26). Since $\boldsymbol{D_x}^T = \boldsymbol{D_y}$, as deducible from (27) and (28), also the matrices $(\boldsymbol{Q_x - D_x Q_y^{-1} D_y})$ and $(\boldsymbol{Q_y - D_y Q_x^{-1} D_x})$ are symmetric. Tailored algorithms exist for the inversion of symmetric matrices, which allow the process to run in a relatively short time.

IV. Validation

Two plane cases of structures with a strong stress concentration supply a robust test bench for the proposed method: a plate with a single hole in traction and a planar structure under compression with three holes drilled. For both geometries, a series of FEM analyses allowed to test the convergence up to a very fine mesh considered as golden standard (GS). The mesh size is controlled by the number of elements along a quarter of the hole circumference. In [40] the upscaling of FEM results occurred thanks to the enhanced continuity of the RBF interpolator. Here, the process is controllable with the number of spare points and it relies on local balance, further than on the favourable mathematical

properties of RBF. The adopted kernel for both methods relying on RBF is the generalized multiquadratics (GMQ) with $q = 1.5$, $R = 0.1$, $\epsilon = 1$ for the plate and $\epsilon = 0.1$ for the rib. The FEM framework used to produce numerical results is Ansys APDL.

FEM results for the GS are compared with the ones obtained with the proposed method. The quality of the output is verified globally, over an area around the geometrical singularity. For this assessment, stress evaluation at the nodes of the GS mesh proceeded employing the proposed method. In this way, the point-wise difference with the GS FEM value gives an error for each stress component. The L2 norm of the vector containing all these quantities is normalized on the L2 norm of the vector with GS nodal stresses, to measure the global error. The same procedure holds to compute the global error also for the RBF method described in [40] and when original FEM stresses are interpolated at GS nodes by means of shape functions.

Addition of spare points follows a systematic workflow, which makes use of Delaunay triangulation. Triangular patches are built using FEM nodes, additional spare points are the centroids of the generated triangles. This process leads to the construction of a sufficiently ordered grid, without the risk of generating coincident points, both vital requirements for a satisfactory RBF interpolation. An excessive number of additional points leads to the ill conditioning of the matrices containing Euclidean correlations.

A strong advantage of the method is that the addition of spare points can affect only critical areas, like the ones hosting stress concentrations, with a wise usage of computational resources. A more extensive validation of the proposed method, including effects on the stress peak value and pros and cons related to the introduction of additional points, can be found in [41].

A. Hole in a plate under traction

This case is the same first analysed in [40], for sake of completeness dimensions are reported below:

- B = base = 30 mm
- H = height = 15 mm
- d = diameter of the hole = 10 mm

The nominal tensile stress is 1000 MPa, which is the traction applied at the boundary. The geometry has two axes of symmetry, which allows the numerical model to be just a quarter of the whole structure, given proper constraints at the boundaries (Fig. 1). Three-noded triangular elements were used (SHELL41) with stiffness only on the plane of definition and unitary thickness. The area in which additional points are introduced is restrained at a radius of 10 mm around the hole centre.

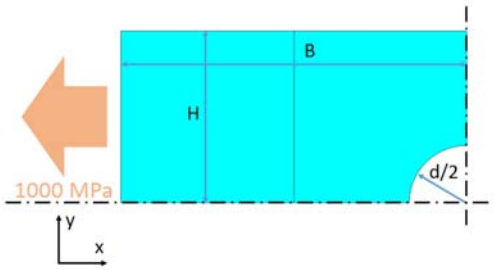

Fig. 1 APDL case geometry for the plate with one centered hole

B. Wing rib with three lightening holes under compressive load

The second case addressed is a flat wing rib with three lightening holes drilled [40], [57]. Also in this case it is possible to take advantage of the double symmetry of the structure, reducing the extension of the numerical counterpart. The dimensions of the model are

- H1 = 196.5 mm, height of the left edge and of module 1 and 2
- H2 = 229.5 mm, height of the right edge
- d = 200 mm, diameter of the holes
- B1 = 393 mm, base of module 1, two times the base of module 2
- B2 = 627 mm, base of the model

A dimensioned sketch of the rib is in Fig. 2.

SHELL41, 4-noded quadrilateral elements with unitary thickness were deployed for the discretization of the model. The rib is subject to a compressive load of 100 MPa, acting along the curved edge. In Fig. 3 the coloured map obtained for the GS is visible, showing the x-component of the stress (σ_x). The RBF post-processing method is applied to both module 1 and module 2 (highlighted in Fig. 2), including stress raisers of different severities. The areas concerned with point addition are the circular belts around the holes, with external radius 150 mm.

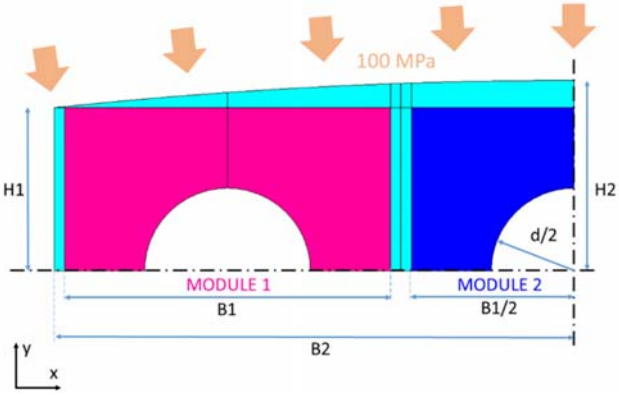

Fig. 2 APDL case geometry for the rib with three lightening holes

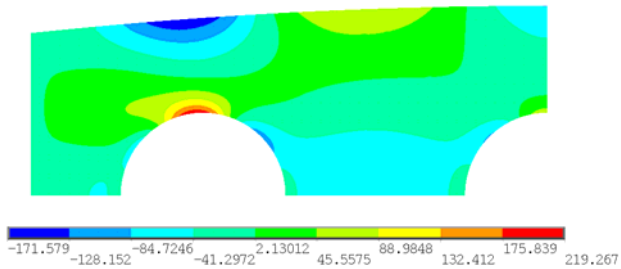

Fig. 3 stress level curves for σ_x obtained by the FEM model for the rib with three lightening holes

We used meshes with an increasing level of refinement to retrieve FEM data necessary to run the method. The procedure is assessed considering the global accuracy of the full stress field.

quarter of the hole, the second and third columns list the percentage errors with respect to GS for FEM interpolation of stresses (by means of shape functions) and for the RBF method. The case of RBF + LB is shown in column four. For all the analysed instances, RBF + LB proved effective in reducing the global error with respect to concurrent methods, even if its action is restricted to a limited portion around the holes. Fig. 4 reports a comparison of stress maps for σ_x against the GS (c). In a), σ_x obtained with APDL for the model with 6 divisions of the hole edge is interpolated at the nodes of the GS mesh by means of triangular shape functions. b) and d) show σ_x maps as output of RBF and RBF + LB methods respectively. The introduction of LB gave the stress contour in correspondence of the hole an aspect more similar to GS with respect to the case of plain RBF.

The proposed procedure combining RBF and balance equations achieved the lowest global errors for all the considered examples.

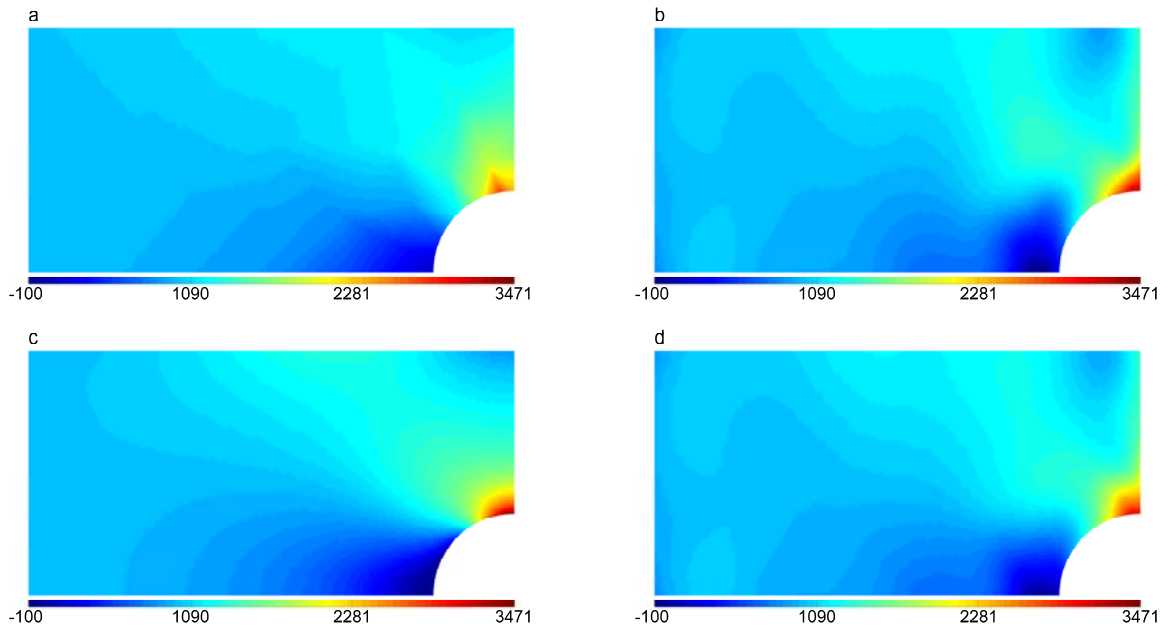

Fig. 4 stress level curves of σ_x for the plate with one centred hole. a) σ_x obtained with FEM for 6 subdivision of the hole edge is interpolated at GS nodes using triangular shape functions. b) σ_x obtained with RBF, input displacements are from the model with 6 subdivisions of the hole edge. c) σ_x obtained with FEM for the GS mesh. d) σ_x obtained with RBF + LB. Input data are the same of c.

C. *Validation results*

The application of the method involving RBF + LB leads to an evolution of the stress contour affecting a certain area, it seemed relevant to investigate the quality of the modified stress field with respect to a reference, throughout the whole portion considered. Table 2 refers to the plate with a hole in traction. Table 3 reports the results for module 1 of the drilled rib, Table 4 exposes the results for module 2 in the same way. The first column from left reports the level of discretization of the starting mesh given as the number of subdivisions along a

Matrix inversions for the methods based on RBF are performed thanks to the tool embedded in the MATLAB Arithmetic Package, which exploits the Cholesky decomposition or the LDL decomposition, a closely related variant of the classical Cholesky decomposition.

Table 2 plate with a hole in traction. Global errors

Subdivisions of the hole's edge	L2 error % FEM	L2 error % RBF	L2 error % RBF+LB
4	24.60%	24.15%	23.86%
6	21.63%	21.74%	19.52%
8	12.69%	11.38%	10.26%
10	10.90%	9.88%	8.49%

Table 3 wing rib, module 1. Global errors

Subdivisions of the hole's edge	L2 error % FEM	L2 error % RBF	L2 error % RBF+LB
4	24.58%	26.61%	23.35%
6	15.48%	14.99%	12.92%
8	11.04%	10.33%	8.71%
10	14.04%	7.52%	6.06%

Table 4 wing rib, module 2. Global errors

Subdivisions of the hole's edge	L2 error % FEM	L2 error % RBF	L2 error % RBF+LB
4	20.19%	24.28%	20.62%
6	12.98%	13.76%	10.79%
8	9.14%	8.81%	6.84%
10	7.03%	6.34%	4.76%

V. J-INTEGRAL EVALUATION

A. Computation of the J-Integral

The J-integral was introduced by Rice [58] and can be calculated as:

$$J = \int_A \left[\sigma_{ij} u_{j,1} - W\delta_{1i}\right] q_{1,i}\, dA \qquad (30)$$

Where W is the stress work energy density, σ_{ij} and u_j are the stress and displacement components, q_1 is an arbitrary function, A is an annular portion including the crack-tip. Several forms are suggested in literature for the J-integral calculation, comprising of linear, surface and volume forms [59]. For a 2D case, the surface integral form (30) demonstrates higher stability and can benefit from a stress state known at a wider surface, not requiring the exact pointwise values of stress immediately around the crack tip. Dealing with a very coarse application, in which the stress results are approximated with respect to analytical results, the surface integral approach of the above form was employed as suggested by [60]. The surface integral domain is evaluated over any closed looped surface around the crack-tip as shown in Fig. 5.

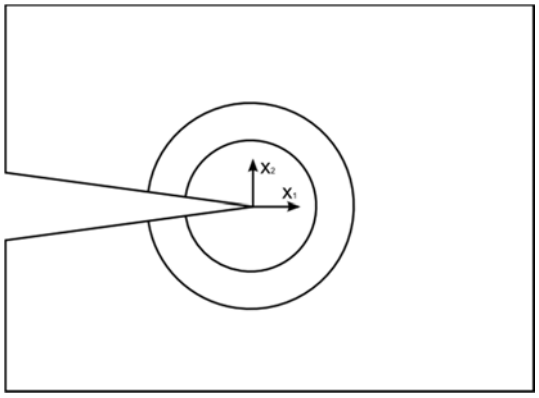

Fig. 5 annular portion around a crack-tip in a thin plate

The only prescription for the function q_1 is to smoothly blend from a unitary value at the inner radius to a null value at the outer circumference. A semi-analytical meshless approach was then developed using RBF for the evaluation of the terms appearing in equation (30). As previously proposed, RBF alone can interpolate FEM displacements at nodes and, given their analytical form, be differentiated to obtain strain and stress fields, otherwise additional points are introduced aiming at enhanced local balance by means of equilibrium in the strong form. Both analytical formulations based on RBF, the simple and the enriched one, are suitable to easily supply all the terms required for Eq (30). As regards the arbitrary q_1 function, it seemed reasonable to choose the same RBF kernel employed for the interpolation of displacements, which was determined once defined the desired values at source points along the boundaries of the annular sector. Exploiting the meshless properties of RBF, the target points for the semi-analytical calculation of Eq.(30) were organized according to a regular grid contained in a annular subdomain as shown in Fig. 6.

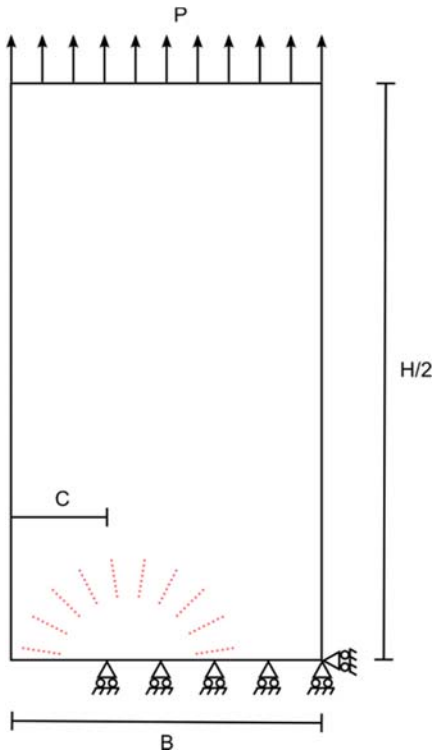

Fig. 6 case geometry for the plate with a side crack with highlighted in red the points employed for J-integral calculation

B. Fracture mechanics test case

The RBF-based upscaling method described was tested on a literature benchmark involving a mode I crack opening on a rectangular plate. Referring to [61], the reference J-integral value was retrieved for the structure shown in Fig. 6 whose dimensions are:

- B = base = 2 m
- H = height = 8 m
- C = crack extension = 0.5 m

The uniformly distributed tearing load at both extremities is P = 10^6 N. To better demonstrate the proposed procedure on very coarse meshes not suitable to be employed for fracture mechanics calculation, a regularly spaced, quadrilateral grid was used to represent the computational domain also near the crack tip, using 4-nodes linear SHELL41 plate elements. Several mesh densities were considered to properly test the method, comparing the outcomes in terms of J-integral with the same mesh but modelled with parabolic SHELL183 plate elements. The adopted kernel was the generalized multiquadratics (GMQ) with q = 1.5, R = 0.1, ϵ = 1.

The J-integral calculation, as shown in the previous paragraph, was performed employing different paths to test the robustness of the algorithm. Both procedures, RBF and RBF+LB are employed to evaluate the values of J-integral. The technique enhancing local balance adopted as additional points the centroids of the patches obtained by triangulating FEM nodes. The proposed post-processing method, requiring points augmentation is performed over a reduced portion, 1 m high from the crack tip. Several plots moving the center of the annular sector away from the crack-tip are reported from Fig. 7 to Fig. 10 where J-integral values are reported versus the element edge of the starting FEM meshes. In the same graphs, FEM evaluations of J-integral from the parabolic mesh adopting the same element distribution are showed for comparison. RBF proved effective in converting scattered FEM results to a continuous form enabling a semi-analytical evaluation of the J-integral. The upgraded procedure embedding local balance succeeded in increasing the reliability of RBF results, moving results closer to the reference benchmark most of the times. Results computed over sectors closer to the crack-tip are more accurate with respect to reference value, at a larger distance a loss in accuracy is observed but a convergent behavior of the output with respect to mesh spacing appears. Elapsed times to run the procedures based on RBF interpolation on such coarse meshes are extremely short: 0.003 s for plain RBF and 0.035s for RBF+LB considering an element edge of 0.2 m. Larger numbers of additional points were tried leading to negligible progress with respect to reported results, with the only effect of longer computational times, thus discussion is omitted.

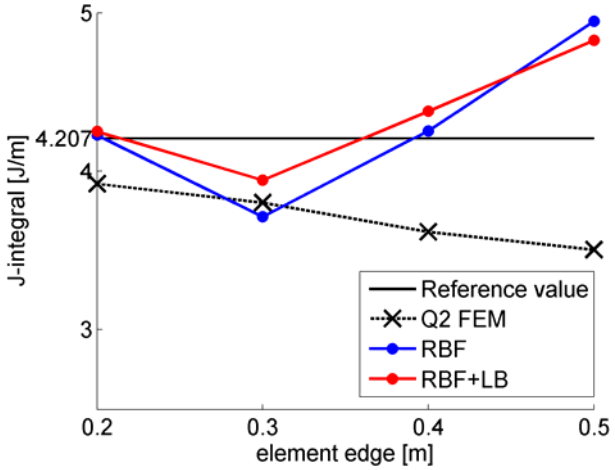

Fig. 7 values of J-integral extracted with FEM deploying quadratic elements, RBF and RBF+LB are compared to the reference value. The annular portion is at a distance of 0 m from the crack-tip, inner radius is 0.2 m, outer radius is 0.45 m

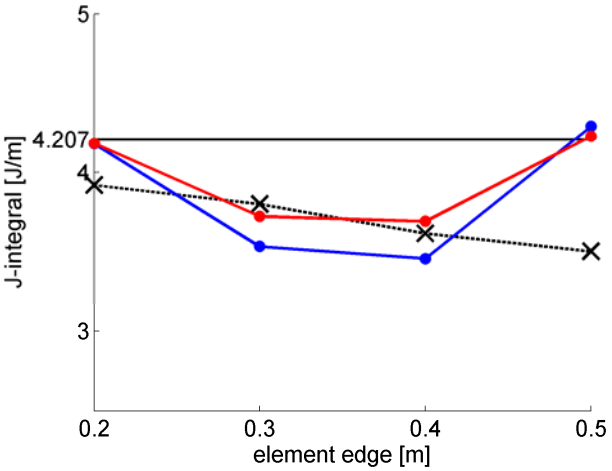

Fig. 8 values of J-integral extracted with FEM deploying quadratic elements, RBF and RBF+LB are compared to the reference value. The annular portion is at a distance of 0.067 m from the crack-tip, inner radius is 0.267 m, outer radius is 0.517 m

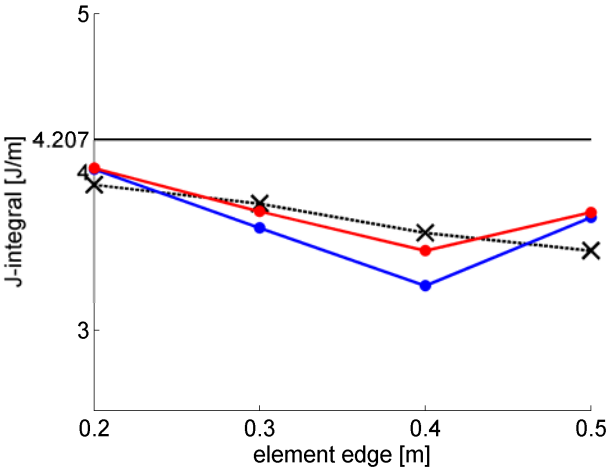

Fig. 9 values of J-integral extracted with FEM deploying quadratic elements, RBF and RBF+LB are compared to the reference value. The annular portion is at a distance of 0.13 m from the crack-tip, inner radius is 0.33 m, outer radius is 0.58 m

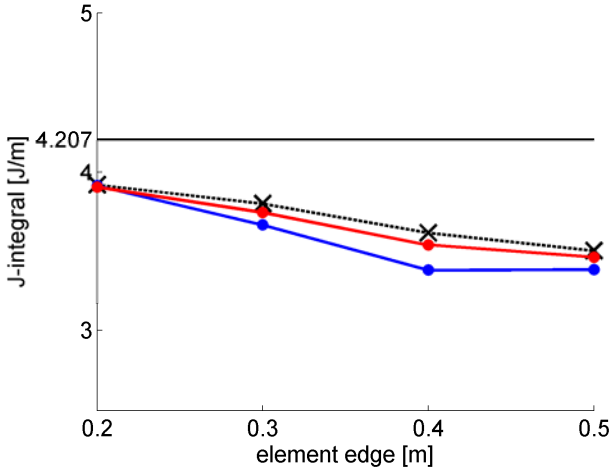

Fig. 10 values of J-integral extracted with FEM deploying quadratic elements, RBF and RBF+LB are compared to the reference value. The annular portion is at a distance of 0.2 m from the crack-tip, inner radius is 0.4 m, outer radius is 0.65

Finer meshes were excluded since a higher proximity of nodes exacerbates the discontinuity starting from the crack-tip, which clashes with the smoothness of RBF approximation [62]. Tests conducted showed that such a strong singularity can be absorbed as long as a buffer distance is kept between RBF centers, with still a good consistency of the derived fields.

VI. Conclusions

In this paper a method to improve the stress state on a 2D FE coarse linear mesh for fracture mechanics applications was shown. By taking as input the displacements obtained on a coarse mesh from a FEM structural analysis, results are processed using a technique based on RBF interpolation which enforces balance in strong form. New points are added to the plain RBF interpolation to enhance equilibrium. After a prior validation on two 2D structural cases involving strong stress concentrations, a fracture mechanics application aiming at the determination of the J-integral was tackled. Proposed procedure demonstrated to be suitable for the J-integral determination on cases in which the coarse Q1 numerical grid is not suitable for fracture mechanics applications, obtaining results comparable to the ones achieved by using higher-order elements. Such method, being meshless, can be employed as a local inspection tool only where needed and even after structural analyses run.

References

[1] Griffith, A.A., 1921. Vi. the phenomena of rupture and flow in solids. Philosophical transactions of the royal society of london. Series A, containing papers of a mathematical or physical character 221, 163–198.)

[2] Ingraffea, A., 1977. Nodal grafting for crack propagation studies. International Journal for Numerical Methods in Engineering 11, 1185–1187.

[3] Mi, Y., Aliabadi, M., 1994. Three-dimensional crack growth simulation using bem. Computers & Structures 52, 871–878

[4] Portela, A., Aliabadi, M., Rooke, D.P., 1993. Dual boundary element incremental analysis of crack propagation. Computers & Structures 46,237-247

[5] Belytschko, T., Black, T., 1999. Elastic crack growth in finite elements with minimal remeshing. International journal for numerical methods in engineering 45, 601–620

[6] T.-P. Fries, T. Belytschko, "The extended/generalized finite element method: an overview of the method and its applications," *International Journal for Numerical Methods in Engineering*, vol. 84, no. 3, pp. 253–304, 2010.

[7] O. C. Zienkiewicz, R. L. Taylor, J. Z. Zhu, *The finite element method: its basis and fundamentals*, 6th edition, Butterworth-Heinemann, 2005.

[8] M. Griebel, M.A. Schweitzer, "A particle-partition of unity method for the solution of elliptic, parabolic and hyperbolic PDEs," *SIAM J. Sci. Comput.*, vol. 22, pp. 853–890, 2000.

[9] K.-C. Kwon, S.-K. Youn, "The least-squares meshfree method for rigid-plasticity with frictional contact," *International Journal of Solids and Structures*, vol. 43, pp.7450–7841, 2006.

[10] B. N. Rao, S. Rahman, "An efficient meshless method for fracture analysis of cracks," *Computational Mechanics*, vol. 26, pp. 398–408, 2000.

[11] T. Belytschko, Y. Krongauz, D. Organ, M. Fleming, P. Krysl, "Meshless methods: An overview and recent developments," *Comput. Methods Appl. Mech. Engrg.*, vol. 139, pp. 3–47, 1996.

[12] L.B. Lucy, "A numerical approach to the testing of the fission hypothesis," *Astron. J.*, vol. 82, pp. 1013–1024, 1977.

[13] L. D. Libersky, A.G. Petscheck, T.C. Carney, J.R. Hipp, F.A. Allahdadi, "High strain Lagrangian hydrodynamics," *J. Comput. Phys.*, vol. 109, pp. 67–75, 1993.

[14] B. Nayroles, G. Touzot, P. Villon, "Generalizing the finite element method: Diffuse approximation and diffuse elements," *Computational Mechanics*, vol. 10, pp. 307–318, 1992.

[15] T. Belytschko, Y. Y. Lu, L. Gu, "Element-free Galerkin methods," *International Journal For Numerical Methods In Engineering*, vol. 37, pp. 229–256, 1994.

[16] I. Babuška, J. M. Melenk, "The partition of unity method," International Journal for Numerical Methods In Engineering, vol. 40, pp. 727–758, 1997.

[17] S. N. Atluri, T. Zhu, "A new meshless local Petrov–Galerkin (MLPG) approach in computational mechanics," Comput. Mech., vol. 22, pp. 117–127, 1998

[18] P. J. Davis, *Interpolation and approximation*, Blaisdell, London, 1963

[19] E. J. Kansa, "Multiquadrics scattered data approximation scheme with applications to computational fluid-dynamics I, surface approximations and partial derivative estimates," *Comput. Math. Appl.*, vol. 19, pp. 127–145, 1990

[20] A. Ali, S. Islam, S. Haq, "A computational meshfree technique for the numerical solution of the two-dimensional coupled Burgers' equations," *Int. J. Comput. Methods Eng. Sci. Mech.*, vol. 10, pp. 406–412, 2009.

[21] Hu, Z.-C. Li, A.-D. Cheng, "Radial basis collocation methods for elliptic boundary value problems," *Comput. Math. Appl.*, vol. 50, pp. 289–320, 2005

[22] B. Šarler, "A radial basis function collocation approach in computational fluid dynamics," *Comput. Model. Eng. Sci.*, vol. 7, pp. 185–193, 2005.

[23] B. Šarler, R. Vertnik, "Meshfree explicit local radial basis function collocation method for diffusion problems," *Comput. Math. Appl.*, vol. 51, pp. 1269–1282, 2006.

[24] C.K. Lee, X. Liu, S.C. Fan, "Local multiquadric approximation for solving boundary value problems," *Comput. Mech.*, vol. 30, pp. 396–409, 2003.

[25] G. Kosec, B. Šarler, "Local RBF collocation method for Darcy flow," *Comput. Model. Eng. Sci.*, vol. 25, no. 3, pp. 197–207, 2008.

[26] G. Fasshauer, *Solving partial differential equations by collocation with radial basis functions, surface fitting and multiresolution methods*, Nashville, USA, Vanderbilt University Press, 1997.

[27] Q. H. Qin, H. Wang, V. Kompis, *MFS with RBF for thin plate bending problems on elastic foundation. Recent Advances in Boundary Element Methods*, Manolis G D, Polyzos D, eds., New York: Springer Science, 2009, pp. 367–378.

[28] M. A. Golberg, C. S. Chen, H. Bowman, H. Power, "Some comments on the use of Radial Basis Functions in the Dual Reciprocity Method" *Computational Mechanics*, vol. 21, pp. 141–148, 1998.

[29] J. G. Wang, G. R. Liu, "A point interpolation meshless method based on radial basis functions," *International Journal for Numerical Methods in Engineering*, vol. 54, pp. 1623–1648, 2002.

[30] J. G. Wang, G. R. Liu, "On the optimal shape parameters of radial basis functions used for 2-D meshless methods," *Computer methods in applied mechanics and engineering*, vol. 191, pp. 2611–2630, 2002.

[31] Brighenti, Roberto. "Application of the element-free Galerkin meshless method to 3-D fracture mechanics problems." Engineering Fracture Mechanics 72.18 (2005): 2808-2820.
[32] Fleming, M., et al. "Enriched element-free Galerkin methods for crack tip fields." International journal for numerical methods in engineering 40.8 (1997): 1483-1504.
[33] Tanaka, Satoyuki, et al. "Analysis of cracked shear deformable plates by an effective meshfree plate formulation." Engineering Fracture Mechanics 144 (2015): 142-157.
[34] Belytschko, Ted, Lei Gu, and Y. Y. Lu. "Fracture and crack growth by element free Galerkin methods." Modelling and Simulation in Materials Science and Engineering 2.3A (1994): 519.
[35] Khosravifard, A., et al. "Accurate and efficient analysis of stationary and propagating crack problems by meshless methods." Theoretical and Applied Fracture Mechanics 87 (2017): 21-34.
[36] Nguyen, Nha Thanh, et al. "Crack growth modeling in elastic solids by the extended meshfree Galerkin radial point interpolation method." Engineering analysis with boundary elements 44 (2014): 87-97.
[37] Gu, YuanTong, et al. "An enriched radial point interpolation method (e-RPIM) for analysis of crack tip fields." Engineering Fracture Mechanics 78.1 (2011): 175-190.
[38] Biancolini, M., Chiappa, A., Giorgetti, F., Porziani, S., Rochette, M., 2018. Radial basis functions mesh morphing for the analysis of cracks propagation. Procedia Structural Integrity 8, 433–443.
[39] Giorgetti, F., Cenni, R., Chiappa, A., Cova, M., Groth, C., Pompa, E., Porziani, S., Biancolini, M.E., 2018. Crack Propagation Analysis of Near-Surface Defects with Radial Basis Functions Mesh Morphing, in: Procedia Structural Integrity, pp. 471–478
[40] A. Chiappa, P. Salvini, C. Brutti, M. E. Biancolini, "Upscaling 2D finite element analysis stress results using radial basis functions," *Computers & Structures*, vol. 220, pp. 131–143, 2019.
[41] Chiappa, A., Groth, C., Biancolini, M.E., 2019. Improvement of 2D finite element analysis stress results by radial basis functions and balance equations. International Journal of Mechanics 13, 90–99
[42] M. D. Buhmann, *Radial Basis Functions: Theory and implementation*, Cambridge Monographs on Applied and Computational Mathematics, Cambridge University Press, 2004.
[43] M. E. Biancolini, *Fast radial basis functions for engineering applications*, Springer, 2018.
[44] S. Haykin, *Neural network: a comprehensive foundation*, 2nd edition, Prentice-Hall, Englewood Cliffs, NJ, 1999.
[45] G. Casciola, D. Lazzaro, L. B. Montefusco, S. Morigi, (2006) "Shape preserving surface reconstruction using locally anisotropic radial basis function interpolants," *Computer and Mathematics with Applications*, vol. 51, no. 8, pp. 1185–1198, 2006.
[46] M. E. Biancolini, "Mesh morphing and smoothing by means of radial basis functions (RBF): a practical example using fluent and RBF morph," in: *Handbook of research on computational science and engineering: theory and practice*. IGI Global, 2011 pp. 347–380.
[47] A. De Boer, M. S. Van der Schoot, H. Bijl, "Mesh deformation based on radial basis function interpolation," *Computers and Structures*, vol. 85, no. 11–14, pp. 784–795, 2007.
[48] M. E. Biancolini, P. Salvini, "Radial basis functions for the image analysis of deformations," in: *Computational Modelling of Objects Represented in Images: Fundamentals, Methods and Applications III Proceedings of the International Symposium*, CRC Press, 2012, pp. 361–365
[49] M. E. Biancolini, A. Chiappa, F. Giorgetti, C. Groth, U. Cella, P. Salvini, "A balanced load mapping method based on radial basis functions and fuzzy sets," *International Journal For Numerical Methods In Engineering*, vol. 115, no. 12, pp. 1411–1429, 2018.
[50] M. E. Biancolini, U. Cella, C. Groth, M. Genta, "Static aeroelastic analysis of an aircraft wind-tunnel model by means of modal RBF mesh updating," *Journal of Aerospace Engineering*, vol. 29, no. 6, 2016
[51] M. E. Biancolini, E. Costa, U. Cella, C. Groth, G. Veble, M. Andrejasic, (2016) "Glider fuselage-wing junction optimization using CFD and RBF mesh morphing," *Aircraft Engineering and Aerospace Technology*, vol. 88, pp. 740–752, 2016.
[52] C. Groth, A. Chiappa, M. E. Biancolini, "Shape optimization using structural adjoint and RBF mesh morphing," *Procedia Structural Integrity*, vol. 8, pp. 379–389, 2018
[53] P. P. Valentini, M. E. Biancolini, "Interactive sculpting using augmented-reality, mesh morphing, and force feedback: force-feedback capabilities in an augmented reality environment," *IEEE Consumer Electronics Magazine*, vol. 7, no. 2, pp. 83–90, 2018.
[54] P. B. Boyd, K. W. Gildersleeve, "Numerical experiments on the condition number of the interpolation matrices for radial basis functions," *Applied Numerical Mathematics*, vol. 61, pp. 443–459, 2011.
[55] W. Pilkey, D. Pilkey, *Peterson's stress concentration factors*, J.Wiley & Sons, 2008.
[56] R. C. J. Howland, *On the stress in the neighbourhood of a circular hole in a strip under tension*, Phil.Trans.Royal Society, London, 1930.
[57] U. Cella, M. E. Biancolini, C. Groth, A. Chiappa, D. Beltramme, "Development and validation of numerical tools for FSI analysis and structural optimization: the EU "Ribes" project status," *AIAS Congress*, Messina, Italy 2015
[58] Rice, James R. "A path independent integral and the approximate analysis of strain concentration by notches and cracks." Journal of applied mechanics 35.2 (1968): 379-386.
[59] Anderson, Ted L., and Ted L. Anderson. Fracture mechanics: fundamentals and applications. CRC press, 2005.
[60] Shih, C. F., B. Moran, and T. Nakamura. "Energy release rate along a three-dimensional crack front in a thermally stressed body." International Journal of fracture 30.2 (1986): 79-102.
[61] Juvinall, Robert C., and Kurt M. Marshek. Fundamentals of machine component design. J. Wiley, 1991.
[62] Wang, Lihua, Jiun-Shyan Chen, and Hsin-Yun Hu. "Subdomain radial basis collocation method for fracture mechanics." International journal for numerical methods in engineering 83.7 (2010): 851-876.